

Importance of iron as the metal ion in peptide deformylase: a biomimetic computational study

Matthew F. Brown · Benjamin F. Gherman

Received: 26 July 2010 / Accepted: 14 September 2010 / Published online: 25 September 2010
© Springer-Verlag 2010

Abstract Peptide deformylase (PDF), a metalloamidase which catalyzes a deformylation step during eubacterial protein biosynthesis, shows a peculiar preference for Fe^{II} as its active site metal ion (in particular, as opposed to Zn^{II} , which is far more common among this class of enzymes). In order to explore the origin of this preference, density functional theory (DFT) calculations have been carried out using a biomimetic heteroscorpionate $\text{N}_2\text{S}_{\text{thiolate}}$ ligand system (L) and the metal centers Fe^{II} , Zn^{II} , and Co^{II} . Comparison of computed ML(formate) complexes to crystal structures of PDF–formate complexes illustrates the viability of the biomimetic ligand for investigating the PDF chemistry. pK_a calculations on $[\text{ML}(\text{H}_2\text{O})]^+$ complexes show that the metal centers are effective Lewis acids in activating the water molecule to allow formation of a nucleophilic hydroxide ligand. Computed oxidation potentials predict the ML(OH) and ML(formate) complexes not to be unstable with respect to oxidation. However, while each of the metal centers was therefore seen to be suitable for PDF chemistry, examination of the entire deformylation reaction showed Fe^{II} to be uniquely suited to PDF. The deformylation reaction was thermodynamically and kinetically optimal with Fe^{II} as the metal center. This is attributed to the charge transfer that occurs from the thiolate ligand to the Fe^{II} center during the reaction and to the relative coordinative flexibility of Fe^{II} that allows for facile interconversion between tetra- and pentacoordination,

leading to greater activation of the substrate carbonyl at the nucleophilic attack transition state.

Keywords Density functional calculations · Peptide deformylase · Reaction thermodynamics · Metalloenzymes

1 Introduction

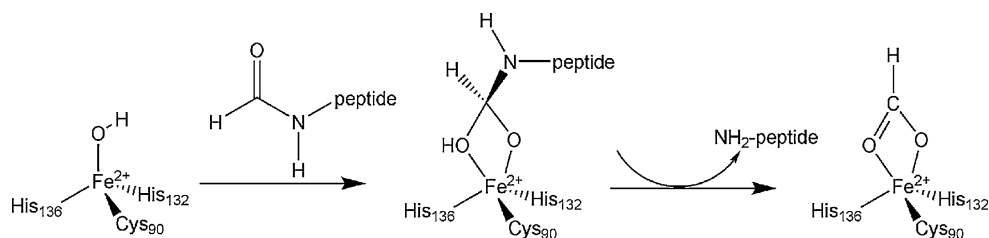
Peptide deformylase (PDF) catalyzes the hydrolytic cleavage of the formyl group at the N-terminus of nascent eubacterial proteins during protein synthesis [1–4]. As PDF is essential for bacterial survival, PDF constitutes a promising target for a new class of antibacterial agents [5–7], making investigation into the structure and function of PDF an important endeavor. In addition, human PDF has recently been identified, the inhibition of which prevented growth in 16 cancer cell lines, suggesting that PDF can be considered an anticancer target as well [8]. PDF is also of great interest from the bioinorganic viewpoint as the only example of an iron metalloamidase [9]. Other metallo-peptidases use Zn^{II} as the metal ion, and the structural and functional characteristics of PDF would otherwise indicate that the enzyme belongs in the mononuclear Zn^{II} enzyme family [9–12]. The choice of iron by nature [13] is intriguing considering the inherent instability of Fe^{II} toward oxidation and that PDF catalyzes a non-redox-active reaction.

Crystal structures of the full-length eubacterial protein [1, 14] and NMR study of PDF [15] indicate the metal ligands to be Cys90, His132, and His136 (each of which are conserved in human PDF [16, 17]) in the HEXXH motif and a solvent-derived ligand (either a water molecule or hydroxide ion) [18]. Mutation experiments on the PDF

Electronic supplementary material The online version of this article (doi:10.1007/s00214-010-0827-2) contains supplementary material, which is available to authorized users.

M. F. Brown · B. F. Gherman (✉)
Department of Chemistry, California State University,
Sacramento, 6000 J Street, Sacramento, CA 95819-6057, USA
e-mail: ghermanb@csus.edu

Fig. 1 The PDF active site and proposed catalytic mechanism [14]



enzyme have confirmed that these three residues are essential for catalytic activity [19]. The presence of the cysteine sulfur ligand as part of the mixed N, S environment is rather uncommon; an N or O donor from His or Asp/Glu is more typical in “zinc” metallopeptidases [9]. A network of hydrogen bonds aligns the metal-coordinating ligands [18]. High-resolution crystal structures of PDF have been obtained when Fe^{II} , Co^{II} , and Zn^{II} are present and indicate tetrahedral coordination around the metal center in each case, with no differences in the overall folds and only minor differences in the active sites with the different metal ions [14, 20].

The proposed deacylation mechanism [14] (Fig. 1) begins with nucleophilic attack of the hydroxide ligand on the carbonyl carbon of the N-terminal formyl group of the peptide. This is followed by the transition from a tetrahedral to a five-coordinate metal center and subsequent formation of an enzyme–formate complex. The metal is proposed to function as an electron-withdrawing group to favor deprotonation of the metal-bound water to yield a hydroxide ligand and as a Lewis acid to activate the bound carbonyl substrate, the latter function of which is likely affected by the presence of the cysteine ligand [20]. Interestingly, catalytic activity is reduced by 2–3 orders of magnitude in Zn^{II} -substituted forms, while no significant loss of catalytic efficiency is observed upon Ni^{II} and Co^{II} substitution [3, 14, 21, 22].

A series of mixed quantum mechanics/molecular mechanics (QM/MM) computational studies on the PDF enzyme have sought to explain this unusual metal preference [23–25]. Despite predicting differing degrees of preference for Fe^{II} over Zn^{II} as the metal center (activation barriers for the nucleophilic attack step ranged from 2.2 kcal/mol [24], to ~ 8 kcal/mol [23], to ~ 10 kcal/mol lower [25] with Fe^{II} vs. Zn^{II}), a theme emerged that metal coordination geometric preferences significantly influenced PDF catalytic activity. In particular, direct coordination between the metal and substrate carbonyl, which was determined to occur more readily with Fe^{II} compared to Zn^{II} , was concluded to play a key role in reducing the activation energy for nucleophilic attack. A computational study utilizing a cluster model of the active site, however, predicted generally smaller differences for the activation barrier for the nucleophilic attack step of 0.6–4.9 kcal/mol

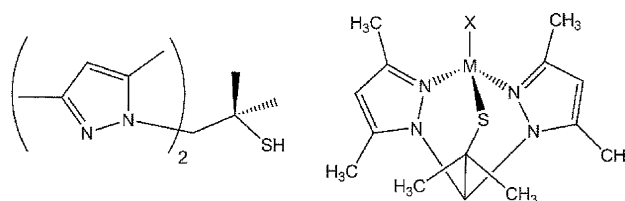


Fig. 2 The heteroscorpionate ligand L by itself and complexed to a metal M and exogenous ligand X

and showed no qualitative differences in geometries along the deacylation reaction coordinate with the different metals [26].

Biomimetic modeling of the PDF active site has provided an alternative means for examining the deacylation reaction catalyzed by PDF. One model developed to this end is the $\text{N}_2\text{S}_{\text{thiolate}}$ ligand, 2-methyl-1-[methyl-(2-pyridin-2-yl-ethyl)amino]propane-2-thiol (or PATH, pyridine–amine–thiolate system) from Goldberg et al. [27–32]. Preliminary density functional theory (DFT) calculations carried out with the PATH ligand system by Goldberg et al. led to conclusions very similar to those seen in the QM/MM studies of PDF [32].

An alternative biomimetic ligand system is the heteroscorpionate ligand [33] bis(3,5-dimethyl-pyrazolyl)(1-methyl-1-sulfanylethyl)methane (L) (Fig. 2) [34, 35]. Both the PATH and L ligands are $\text{N}_2\text{S}_{\text{thiolate}}$ systems bearing an aliphatic thiolate as a mimic of the cysteine donor in PDF and yield monomeric metal complexes. As shown in crystal structures [35], the heteroscorpionate ligand (like the PATH ligand) supports tetrahedral coordination around the metal in $\text{ZnL}(\text{X})$ complexes ($\text{X} = \text{Cl}$, acetate), similar to that seen in the Zn^{II} form of PDF [14, 20]. In addition, and separate from the PATH ligand, the ligand L has been shown to be readily substituted along both the pyrazolyl groups and the pendant arm bearing the thiolate function [35, 36].

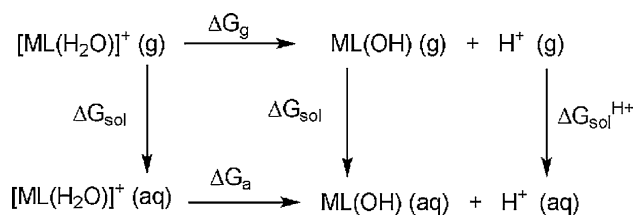
In this work, this heteroscorpionate ligand L combined with DFT computational methods will be used to study the deacylation reaction catalyzed by PDF. The distinguishing goals will be to: (a) demonstrate the capability of current biomimetic ligands to accurately represent the enzyme chemistry; (b) support the importance of Fe^{II} as the catalytically preferable metal ion over Zn^{II} ; and (c) provide

new insights by examining how the identity of the metal affects the chemistry, geometry, and electronic structure of each species involved in the deformylation reaction. We begin first by examining the ability of various density functionals to reproduce the coordination chemistry of the MLX complexes. Following that, the formate complexes of ML (where M = Fe^{II}, Co^{II}, and Zn^{II}) are examined and compared to PDF crystallographic data. We next examine the relative stability of the hydroxide ligand required for the nucleophilic attack and compare the stability of the iron complexes with regard to oxidation to those with cobalt and zinc. Finally, the deformylation reaction with each of the three different metal centers is examined along with the changes in the electronic structure and bonding of the MLX complexes during the reaction. An explanation for the preference for Fe^{II} at the active site of PDF is then seen to emerge from the pool of data presented.

2 Computational methods

All calculations were carried out using density functional theory (DFT) methods as implemented in the PQS ab initio program package [37]. The performance and selection of various density functionals used in this work is detailed in the Sect. 3.1. All geometry optimizations were carried out with the 6-31G(d,p) basis set on all atoms, except the metal center, for which the Stuttgart effective core potential basis set was used [38]. Transition-state geometries were obtained by first determining the reaction coordinate profile, which was achieved by freezing at least one interatomic distance while optimizing all other degrees of freedom. Energetic maxima along the reaction coordinate were then used for all transition-state searches, which proceeded according to an eigenvector-following algorithm [39]. Mulliken charge populations, natural population analysis (NPA) partial atomic charges, and Wiberg bond indices (the latter two from the NBO 5.0 program [40]) were used to track electronic changes during the deformylation reaction. Vibrational frequency calculations were carried out on all optimized geometries and transition-state structures in order to verify the character of these stationary points. These calculations also allowed for zero-point energy, enthalpy, and entropy corrections to be made to the electronic energies, in turn enabling free energies to be determined. Final electronic energies were obtained through single-point energy calculations on the optimized geometries and transition states with the 6-311G(d,p) basis set (except again utilizing the Stuttgart effective core potential basis set for the metal).

Single-point solvation energies for optimized geometries and transition states were computed using COSMO [41–44] with water ($\epsilon = 78.39$) as the solvent. For the



Scheme 1 Born–Haber free-energy cycle used to determine pK_a values

stationary points involved in the deformylation reaction, solvation energies were also computed using $\epsilon = 5.0$, which would more closely represent the dielectric constant in the interior of a protein [45]. A translational entropy correction was included for free-energy changes computed in solution in order to account for the difference in concentration between the 1 atm gas-phase standard-state concentration (equal to 1/24.5 M as determined from the ideal gas law) and the 1 M standard-state solution concentration [46].

pK_a values were determined through the use of a Born–Haber free-energy cycle (Scheme 1). The free-energy change for deprotonation in aqueous solutions is given as follows:

$$\Delta G_a = \Delta G_g + \Delta G_{\text{sol}}^{\text{ML(OH)}} + \Delta G_{\text{sol}}^{\text{H}^+} - \Delta G_{\text{sol}}^{\text{[ML(H}_2\text{O)]}^+} \quad (1)$$

where ΔG_g is the gas-phase deprotonation energy and $\Delta G_{\text{sol}}^{\text{[ML(H}_2\text{O)]}^+}$, $\Delta G_{\text{sol}}^{\text{ML(OH)}}$, and $\Delta G_{\text{sol}}^{\text{H}^+}$ are the solvation energies for conjugate acid and base forms and the proton (the last of which is taken to be -265.9 kcal/mol prior to including the correction for the 1-atm to 1-M standard-state change) [47, 48]. The pK_a is then calculated as follows:

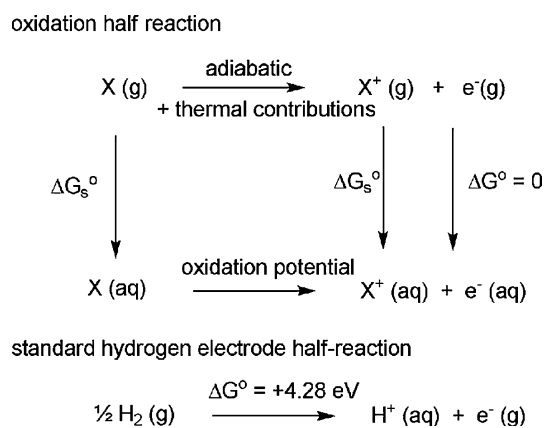
$$\text{pK}_a = \frac{\Delta G_a}{2.303RT} \quad (2)$$

where R is the universal gas constant and T is the temperature. An empirical correction was employed to compensate for systematic error involved in the computation of the pK_a values for the [ML(H₂O)]⁺ complexes. pK_a values were computed for H₃O⁺, CH₃OH₂⁺, and CH₃CH₂OH₂⁺ as well as for H₂O, CH₃OH, and CH₃CH₂OH. Comparison of these computed values with literature pK_a values [49] for these species led to a correction factor of -8.4 units.

Adiabatic oxidation potentials were calculated using a free-energy cycle as well (Scheme 2). The free-energy change for oxidation in solution ΔG_{ox} is

$$\Delta G_{\text{ox}} = G_g^{\text{X}^+} - G_g^{\text{X}} + \Delta G_{\text{sol}}^{\text{X}^+} - \Delta G_{\text{sol}}^{\text{X}} \quad (3)$$

where $G_g^{\text{X}^+}$ and G_g^{X} are the gas-phase free energies for the oxidized and reduced species, and $\Delta G_{\text{sol}}^{\text{X}^+}$ and $\Delta G_{\text{sol}}^{\text{X}}$ are the corresponding solvation energies. The absolute oxidation potential is given as follows:



Scheme 2 Free-energy cycle used to determine adiabatic reduction potentials

$$E^\circ = -\frac{\Delta G_{ox}}{nF} \quad (4)$$

where F is the Faraday constant and n is the number of electrons transferred. The oxidation potential relative to the standard hydrogen electrode (SHE) is obtained by adding 4.28 V to the quantity in Eq. 4 [48].

3 Results

3.1 Assessment of density functionals

A preliminary set of calculations was carried out in order to form an initial connection to experimental data as well as to determine which density functional might be the optimal one to apply to coordination complexes with the heteroscorpionate ligand L . Geometries for $ZnL(\text{acetate})$ and $ZnL(\text{Cl})$ were optimized using six different density functionals—the pure functionals BLYP [50, 51], OLYP [51, 52], and HCTH [53], and the hybrid functionals B3LYP [50, 51, 54], O3LYP [51, 52, 55], and B97-1 [53, 56]. The heavy-atom RMSD between these calculated geometries and those from available crystal structures [35] were determined (Tables 1, 2). In addition, the average difference in metal–ligand bond length was measured between the optimized and crystal geometries for $ZnL(\text{acetate})$ and $ZnL(\text{Cl})$ so as to specifically assess the functionals' ability to reproduce the coordination chemistry around the metal center. With the minimum M–L bond distance deviation from the crystal structures for both Zn complexes and either the smallest (the case of $ZnL(\text{acetate})$) or among the smallest (the case of $ZnL(\text{Cl})$) RMSD versus the crystal structures, the O3LYP geometries were judged to be most optimal. All subsequent calculations therefore utilized the O3LYP functional exclusively.

Table 1 Comparison between $ZnL(\text{acetate})$ geometries optimized with a variety of density functionals and the $ZnL(\text{acetate})$ crystal structure [35]

	Average difference in M–L bond length versus crystal structure (Å)	Heavy-atom RMSD versus crystal structure (Å)
BLYP	0.067	0.057
B3LYP	0.052	0.042
OLYP	0.072	0.061
O3LYP	0.044	0.037
B97-1	0.052	0.044
HCTH	0.069	0.060

Table 2 Comparison between $ZnL(\text{Cl})$ geometries optimized with a variety of density functionals and the $ZnL(\text{Cl})$ crystal structure [35]

	Average difference in M–L bond length versus crystal structure (Å)	Heavy-atom RMSD versus crystal structure (Å)
BLYP	0.067	0.055
B3LYP	0.045	0.042
OLYP	0.070	0.012
O3LYP	0.045	0.043
B97-1	0.046	0.043
HCTH	0.067	0.067

3.2 Formate complexes of ML

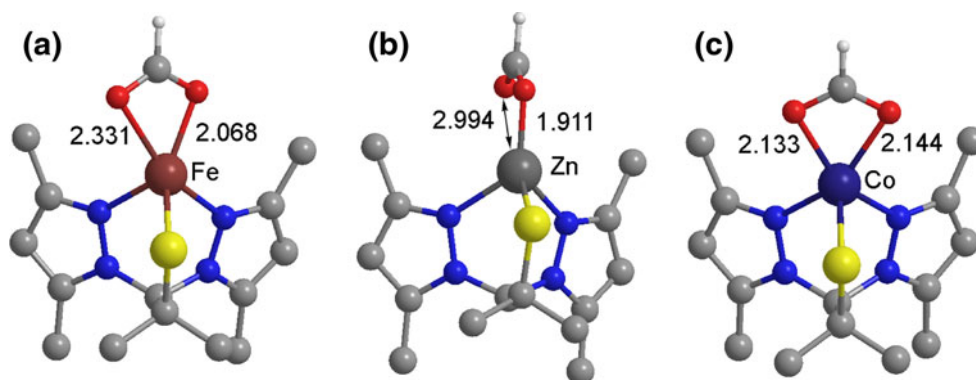
Along with the deformed peptide, the other product of the deformylation reaction is a formate complex ML(formate). Optimized geometries for these formate complexes were obtained with the formate ligand in monodentate and bidentate coordination modes with each of the three metals.¹ In the case of Fe^{II} and Co^{II} , which can exhibit multiple spin states (unlike Zn^{II} , which is a singlet only), the formate complexes were obtained for each spin state (singlet, triplet, and quintet for Fe^{II} ; doublet and quartet for Co^{II}). Comparison of the electronic energies for the different spin states of Fe^{II} and Co^{II} (Tables S1, S2) shows the high-spin quintet and quartet states, respectively, to be the lowest in energy regardless of the formate coordination mode.

¹ Coordination by formate (and by carbamic acid in the tetrahedral intermediate structures) was deemed to be bidentate if both metal–oxygen distances were less than 2.35 Å and both metal–oxygen Wiberg bond indices were greater than 0.10. The interaction between the metal center and oxygen atom was considered significant if these two parameters were satisfied. Notably, in each structure characterized as having monodentate formate or carbamic acid coordination, the second metal–oxygen distance was at least 2.85 Å with a Wiberg bond index of ~ 0.02 or less between the two atoms.

Table 3 Relative free energies (25 °C, in water) for formate coordination modes to ML and comparison between computed geometries and crystal structures of PDF bound to formate [20]

	ΔG (kcal/mol) between formate coordination modes ^a	Lowest energy ML(formate) geometry: M–O distances (Å)	PDF crystal structure data: M–O distances (Å)
Iron	–1.47	2.068, 2.331	2.30, 2.44
Cobalt	–5.42	2.133, 2.144	2.30, 2.32
Zinc	+3.56	1.911, 2.994	2.09, 2.88

^a Tabulated as G(bidentate)—G(monodentate)

Fig. 3 Optimized geometries for the lowest energy formate complexes with **a** M = Fe, **b** M = Zn, and **c** M = Co. Hydrogen atoms on L are omitted for clarity. Distances are measured in Å

The bidentate formate coordination mode is most stable for the FeL(formate) and CoL(formate) complexes (high-spin states) by 1.47 and 5.42 kcal/mol, respectively (Table 3). For ZnL(formate), the monodentate coordination mode is lower in energy by 3.56 kcal/mol. These results are consistent with prior reports on the geometric preferences of the formate complexes based upon QM/MM computational studies of the PDF enzyme system itself [23–25]. It is worth noting that the smallest energy difference for the interconversion between monodentate and bidentate isomers occurs with Fe^{II}. Much larger energy differences occur with Zn^{II} and Co^{II} as the metal center, indicating relatively inflexible formate coordination to these metal centers. The tendency for Zn^{II} to prefer being tetra-coordinate here will prove important in the analysis of the deformylation reaction mechanism (vide infra).

The geometries of the lowest energy ML(formate) complexes (Fig. 3) each show a tetrahedral coordination around the metal center. The bidentate FeL(formate) complex has an asymmetry in the two Fe–O distances (a difference of 0.263 Å), while the bidentate CoL(formate) complex has nearly equal Co–O distances. M–O distances in the ML(formate) complexes are systematically shorter (by approximately 0.15 Å) than those observed in the PDF–formate crystal structures with Fe^{II}, Zn^{II}, and Co^{II} (see Table 3) [20]. This difference, though, cannot be attributed to use of the biomimetic model system, as similar differences in both sign and magnitude were seen in prior QM/MM computational work on the PDF enzyme

Table 4 Computed pK_a values for the [ML(H₂O)]⁺ complexes at 25 °C

	pK _a
[FeL(H ₂ O)] ⁺	10.8
[CoL(H ₂ O)] ⁺	9.0
[ZnL(H ₂ O)] ⁺	8.4

[23–25]. Nonetheless, comparison between the two sets of M–O distances clearly reveals that the overall coordination geometry and formate coordination mode for each metal, as well as the two similar Co–O distances and two dissimilar Fe–O distances, all mirror the structural trends of the coordination geometries seen in the PDF–formate crystal structures. This provides an important demonstration that the biomimetic heteroscorpionate ligand can be an effective model for the active site structures observed in the PDF crystal structures.

3.3 pK_a values for [ML(H₂O)]⁺

The first step in the deformylation reaction catalyzed by PDF involves nucleophilic attack of the metal-bound hydroxide onto the terminal carbonyl group of the peptide substrate. The equilibrium between ML(OH) and its conjugate acid [ML(H₂O)]⁺ was therefore assessed. Based upon the lowest energy spin states for the hydroxide and water complexes (Tables S1, S2; again, the high-spin states for Fe^{II} and Co^{II}), the pK_a values for the [ML(H₂O)]⁺ complexes with each metal were determined (Table 4). Each of [FeL(H₂O)]⁺, [CoL(H₂O)]⁺, and [ZnL(H₂O)]⁺ has similar pK_a values,

Table 5 Computed oxidation potentials (in V at 25 °C; relative to the standard hydrogen electrode) for the ML(OH) and ML(formate) complexes

	ML(OH)	ML(formate)
Iron	−0.18	−0.75
Cobalt	−0.77	−1.34
Zinc	−1.27	−1.48

each several units lower than the pK_w value of 14.0 (at 25 °C) [57]. Each of the ML complexes is thus effective as a Lewis acid in polarizing the coordinated water molecule and thereby increasing the acidity of the bound water ligand, or in other words of effecting a relative shift in the acid–base equilibrium from $[ML(H_2O)]^+$ to ML(OH).

3.4 Oxidation potentials for ML complexes

The presence of Fe^{II} as the metal ion in PDF is unusual, as it is a redox-active metal ion being used to catalyze a non-redox reaction. In order to examine the stability of the Fe^{II} complexes with respect to oxidation, the oxidation potentials of $FeL(OH)$ and $FeL(formate)$ were computed and compared to those with Zn^{II} and Co^{II} as the metal center. In particular, the Zn^{II} complexes serve as a useful reference point since Zn^{II} should be highly stable toward oxidation.

The oxidation potentials, reported relative to the standard hydrogen electrode and based upon the lowest energy spin states for the neutral and oxidized species (Tables S1, S2), are shown in Table 5. Oxidation potentials for the ML(formate) complexes are lower than for the ML(OH) complexes, consistent with the greater concentration of charge on the hydroxide ion versus the delocalized charge on the formate ion. The hydroxide ligand is then better able to stabilize the oxidized state of the metal. As expected, the Zn^{II} complexes have the most negative oxidation potential owing to the significant stability of the +2 oxidation state for zinc. The iron formate and hydroxide complexes, while the relatively easiest to oxidize, nonetheless importantly still have negative E° values for oxidation. The Fe^{II} complexes are indicated then not to be unstable toward oxidation and would require an oxidant with a positive reduction potential in order to undergo oxidation.

3.5 Deformylation reaction energetics and electronic structure changes

3.5.1 Reaction thermodynamics

Energetics for the deformylation reaction have been computed with each of the three metal centers (Fe^{II} , Zn^{II} , and Co^{II}). In the cases of Fe^{II} and Co^{II} , the high-spin states have been used exclusively as each of the complexes already

examined with these two metal ions had as its ground state the high-spin state. The model substrate used in the computations was formamide, such that the model deformylation reaction was as follows:



Free energies were computed using both water as the solvent ($\epsilon = 78.39$) and the dielectric constant set to 5.0 (chosen to mimic the approximate dielectric constant at the protein active site) [45]. As there are no significant differences between the two sets of results, the former are discussed here, while the latter are shown in parentheses in Fig. 4. Examination of the overall free-energy change for the deformylation reaction (Fig. 4) reveals that deformylation is most exoergic in the case of Fe^{II} and Co^{II} . In particular, there is a thermodynamic preference of 2.26 kcal/mol for Fe^{II} over Zn^{II} as the metal center.

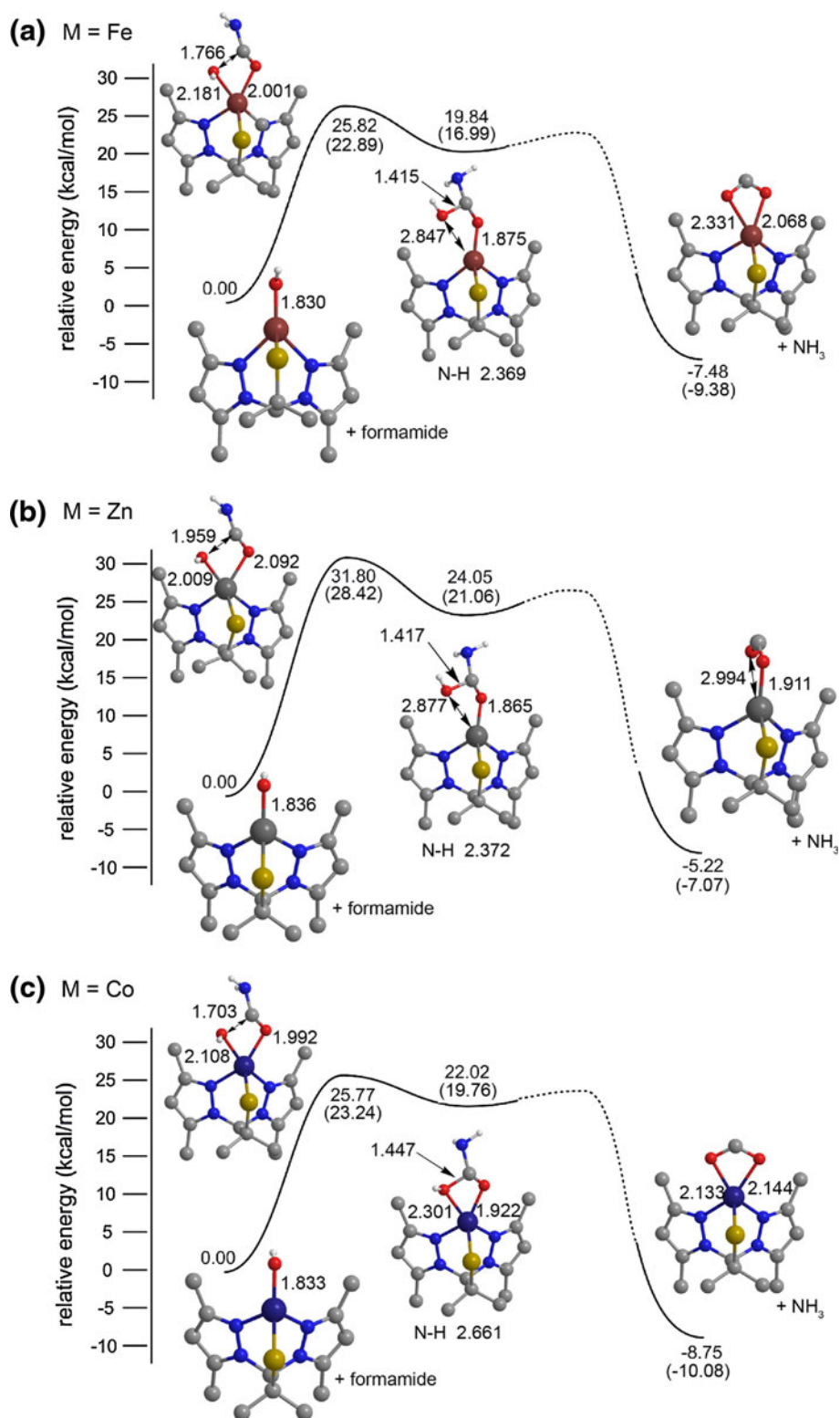
3.5.2 Reaction kinetics

Stationary points along the deformylation reaction coordinate, including the transition state for the nucleophilic attack step and the subsequently formed tetrahedral intermediate, were determined for each metal center (Fig. 4). The proton-transfer step(s) that connect the tetrahedral intermediate to the ML(formate) and ammonia products were not modeled here. This portion of the reaction is not expected to be rate-determining given the experimental dependence of the reaction rate on the identity of the metal center [3, 14]. The proton transfers also cannot be modeled usefully here, as these steps are mediated by hydrogen-bonding groups within the protein active site [14].

With Fe^{II} as the metal ion, the nucleophilic attack transition state has a free energy of activation of 25.82 kcal/mol. The substrate formamide is bound to Fe^{II} at this point with an Fe^{II} –carbonyl O distance of 2.001 Å. The tetrahedral intermediate is then lower in energy by ~ 6 kcal/mol, and the Fe^{II} –carbonyl O distance is shortened to 1.875 Å. The oxygen atom from the metal-bound hydroxide is now distanced from the iron center, resulting in monodentate coordination of the carbamic acid (NH_2COOH) group in the intermediate structure.

The deformylation reaction has several contrasts when Zn^{II} is the metal ion. The activation free energy rises to 31.80 kcal/mol and the metal–carbonyl O distance is longer by 0.091 Å. Based upon transition-state theory, the ~ 6.0 kcal/mol larger reaction barrier with Zn^{II} corresponds to a reaction rate 2.4×10^4 times slower with Zn^{II} versus Fe^{II} , in reasonable agreement with the $\sim 10^3$ -order decrease in PDF catalytic activity observed with the Zn^{II} -substituted forms of the enzyme [3, 14, 21, 22]. Equivalently, it can be observed that the ~ 6.0 kcal/mol difference in activation barrier between the Fe^{II} and Zn^{II} complexes is

Fig. 4 Reaction coordinates for the deformylation reaction displaying the calculated stationary points with **a** $M = \text{Fe}$, **b** $M = \text{Zn}$, and **c** $M = \text{Co}$. Hydrogen atoms on L are omitted for clarity. Distances are measured in Å. Energies shown are relative free energies in water at 25 °C; energies in *parentheses* are relative free energies in a solvent dielectric of $\epsilon = 5.0$ at 25 °C



consistent with the ~ 3.5 kcal/mol difference predicted from transition-state theory based upon the biochemical data for k_{cat} for the Fe^{II} and Zn^{II} forms of PDF. In addition, while the geometry of the tetrahedral intermediate is much

like that of the Fe^{II} case, the intermediate is ~ 4 kcal/mol higher in energy than the Fe^{II} analogue.

In the case of $M = \text{Co}^{\text{II}}$, the nucleophilic attack transition state and free energy of activation are both very close

to those with Fe^{II} (also in accord with the near equivalent catalytic activity observed with the Co^{II}-substituted PDF) [3, 14]. The geometry of the tetrahedral intermediate differs though from both Fe^{II} and Zn^{II}, in that the hydroxide nucleophile remains loosely bound to Co^{II} at a distance of 2.301 Å. The Co^{II} intermediate is ~2 kcal/mol lower in energy than the Zn^{II} intermediate, but also ~2 kcal/mol higher in energy than the Fe^{II} intermediate.

For each of the metal centers, alternative binding modes for the carbamic acid moiety in the tetrahedral intermediate were considered. However, the bidentate coordination mode with Zn^{II} and the monodentate coordination mode with Co^{II} were both unstable under optimization. Only with Fe^{II} was a stable intermediate isomer found. The bidentate isomer in this case was 5.55 kcal/mol higher in energy than the monodentate form. The existence of this isomer does nonetheless provide another indication of the coordinative flexibility (between tetracoordinate and pentacoordinate) with Fe^{II} versus Zn^{II} and Co^{II} as the metal center.

3.5.3 Electronic structure and bonding

In examining the electronic structure and bonding characteristics along the deformylation reaction path, comparison will be restricted to the Fe^{II} and Zn^{II} cases, as these are the most biochemically relevant metal centers. Mulliken charge populations during the course of the reaction (Table 6) show that in proceeding from FeL(OH) to the Fe^{II} transition state, there is a decrease in the magnitude of the charge of the thiolate sulfur atom (by 0.077) along with a slight decrease in the positive charge on iron (by 0.019). Little further change occurs in going to the tetrahedral intermediate. However, upon conclusion of the reaction by formation of the FeL(formate) complex, there is a further decrease in the magnitude of the sulfur and iron charge populations. For the overall reaction, the charge on iron has decreased by 0.040 and the charge on sulfur has increased by 0.116. Perusal of the Mulliken charge populations of the exogenous ligands and the remainder of the heteroscorpionate ligand L confirms that these changes in the iron and sulfur charge populations indeed show charge transfer occurring from sulfur to iron during the course of the

Table 6 Mulliken charge populations along the deformylation reaction pathway for M = Fe, Zn

	M = Fe		M = Zn	
	Fe	S	Zn	S
ML(OH)	0.649	-0.359	0.614	-0.288
Transition state	0.630	-0.282	0.671	-0.330
Tetrahedral intermediate	0.632	-0.285	0.652	-0.290
ML(formate)	0.609	-0.243	0.658	-0.281

Table 7 M–S Wiberg bond indices along the deformylation reaction pathway for M = Fe, Zn

	M = Fe	M = Zn
ML(OH)	0.290	0.368
Transition state	0.376	0.348
Tetrahedral intermediate	0.384	0.369
ML(formate)	0.406	0.346

deformylation reaction. On the other hand, a markedly different trend is seen in the Zn^{II} case. The charge on zinc becomes more positive and the charge on sulfur more negative in going to the transition state from the ZnL(OH) complex. At the end of the reaction, the charge on sulfur is nearly unchanged ($\Delta = +0.007$), while the zinc charge has become slightly more positive ($\Delta = +0.044$). We note that the same changes in charge populations can also be seen if NPA charges are considered (Table S3).

The transfer of charge from sulfur to iron is facilitated by a relatively large increase in the Fe–S Wiberg bond index (Table 7) in going from FeL(OH) to the transition state and a second relatively smaller increase in the Fe–S Wiberg bond index upon formation of the FeL(formate) complex. In contrast, with Zn^{II}, there is a decrease in metal–sulfur bond index between the transition state and ZnL(OH) and then no further net change in metal–sulfur bond index between the transition state and the ZnL(formate) complex. Such metal–thiolate interactions are known to play important roles throughout bioinorganic chemistry [58].

The lower free energy of activation for the nucleophilic attack in the Fe^{II} versus Zn^{II} case can also be attributed to the nature of the interaction of the substrate carbonyl group with the metal center at the transition state. The Wiberg bond index for the Fe–carbonyl O ligation (0.205) is greater than that for the Zn–carbonyl O ligation (0.086) at the transition state, indicating the metal–substrate interaction is almost twice as strong in the Fe^{II} case as in the Zn^{II} case, consistent with the QM/MM studies on the PDF enzyme [23–25]. Even though both the iron and zinc centers are transiently five-coordinate at the transition state, the more flexible coordination environment offered by iron enables the stronger fifth coordination from the substrate carbonyl oxygen. Fe^{II} is then better able to activate the substrate carbonyl group for nucleophilic attack at the transition state. This is confirmed by a longer substrate C=O bond distance (1.284 Å) and lower substrate C=O Wiberg bond index (1.221) in the Fe^{II} transition state than in the Zn^{II} transition state (1.257 Å and 1.360, respectively).

3.6 Comparison to other computational studies on PDF

Despite their different treatment of the PDF enzyme system, the recent computational QM/MM [23–25] and PATH

ligand [32] studies on PDF led to results similar to those obtained with the biomimetic heteroscorpionate ligand system used in the present study. The Fe^{II} form is associated with the lowest activation energy, and the ~ 6 kcal/mol kinetic preference predicted here falls within the 2–10 kcal/mol range from the QM/MM calculations. Further, both the current and previous studies demonstrate that the Fe^{II} metal center can accommodate either tetra- or pentacoordination (with relatively small energetic differences between the two coordination modes), while Zn^{II} has a significant preference for the lower coordination number. This in turn is likewise connected to a stronger and more stabilizing interaction between the substrate and metal center at the transition state in the Fe^{II} case. Importantly, such comparisons support the viability of the current biomimetic model system for studying the chemistry at the PDF active site. As with the earlier computational studies, the present work contrasts with the primary results from the cluster-model study on PDF [26], which had concluded that no significant differences occur with the different metal centers.

4 Conclusions

PDF, a eubacterial enzyme that cleaves the N-terminal formyl group from newly synthesized peptides during protein synthesis, has attracted considerable attention as a new antibacterial target as its function is necessary to bacterial survival. The remarkable aspect of PDF is that, while nearly all other metallopeptidases contain Zn^{II} as the active site metal ion, PDF contains Fe^{II} . Furthermore, the catalytic activity significantly decreases in Zn^{II} -substituted forms of PDF. The question has thus arisen as to why Fe^{II} is more suitable to the reaction catalyzed by PDF than the a priori more likely Zn^{II} .

DFT calculations have been applied here to a heteroscorpionate $\text{N}_2\text{S}_{\text{thiolate}}$ biomimetic ligand system in order to study the deformylation reaction using each of Fe^{II} , Zn^{II} , and Co^{II} as the metal center. After calibrating the choice of density functional to available crystallographic data for Zn^{II} complexes of the biomimetic ligand, the energetics of the deformylation reaction were examined. In addition, the reactant $\text{ML}(\text{OH})$ complexes, the product $\text{ML}(\text{formate})$ complexes, and the electronic changes that occur during the course of the reaction were all characterized.

pK_a calculations for the $[\text{ML}(\text{H}_2\text{O})]^+$ complexes showed that Fe^{II} (as well as Zn^{II} and Co^{II}) could be suitable as the metal center in PDF as per its ability to serve as a Lewis acid in polarizing a coordinated water molecule and stabilizing the conjugate base $\text{ML}(\text{OH})$ complex needed for nucleophilic attack on the peptide substrate. Computed oxidation potentials for $\text{ML}(\text{OH})$ and $\text{ML}(\text{formate})$ were

negative, showing that, even for the case of Fe^{II} , these complexes were not unstable toward oxidation.

Investigation into the energetics associated with the species involved in the deformylation reaction indicated Fe^{II} to be particularly suitable over Zn^{II} as the metal ion in PDF. Of all the $\text{ML}(\text{formate})$ complexes, $\text{FeL}(\text{formate})$ had the smallest free-energy difference between the monodentate and bidentate formate coordination forms and provided evidence of a relative coordinative flexibility between tetra- and pentacoordination in the Fe^{II} complexes. The deformylation reaction was also thermodynamically (by 2.26 kcal/mol) and kinetically (by 5.98 kcal/mol) more favorable with Fe^{II} than with Zn^{II} . The Fe^{II} tetrahedral intermediate was likewise lower in energy than the Zn^{II} analogue by 4.21 kcal/mol.

These energetic differences were attributed to two factors in the electronic structure of the Fe^{II} and Zn^{II} complexes. First, a significant transfer of charge from sulfur to iron occurs during the reaction and is facilitated by an increasing iron–sulfur bond order during the reaction. No such charge transfer occurs in the Zn^{II} case. Second, the coordinative flexibility of iron allows for greater activation of the substrate carbonyl at the nucleophilic attack transition state.

In short, the biomimetic heteroscorpionate ligand system allows for an effective exploration of the metal coordination chemistry which occurs in PDF. The computational results from this model suggest that while both Fe^{II} and Zn^{II} might be generally suitable as metal centers in PDF, the iron center is thermodynamically and kinetically preferred owing to its ability to interchange between tetra- and pentacoordination as well as its particular electronic interactions with its supporting ligands and the peptide substrate.

Acknowledgments This work was funded by the California State University, Sacramento College of Natural Sciences and Mathematics.

References

1. Chan MK, Gong WM, Rajagopalan PTR, Hao B, Tsai CM, Pei DH (1997) *Biochemistry* 36:13904–13909
2. Hao B, Gong WM, Rajagopalan PTR, Zhou Y, Pei DH, Chan MK (1999) *Biochemistry* 38:4712–4719
3. Rajagopalan PTR, Yu XC, Pei DH (1997) *J Am Chem Soc* 119:12418–12419
4. Yuan Z, White RJ (2006) *Biochem Pharmacol* 71:1042–1047
5. Leeds JA, Dean CR (2006) *Curr Opin Pharmacol* 6:445–452
6. Winum J-Y, Kohler S, Scozzafava A, Montero J-L, Supuran CT (2008) *Anti-Infect Agents Med Chem* 7:169–179
7. Giglione C, Pierre M, Meinel T (2000) *Mol Microbiol* 36:1197–1205
8. Lee MD, She Y, Soskis MJ, Borella CP, Gardner JR, Hayes PA, Dy BM, Heaney ML, Philips MR, Bornmann WG, Sirotnak FM, Scheinberg DA (2004) *J Clin Invest* 114:1107–1116

9. Lipscomb WN, Strater N (1996) *Chem Rev* 96:2375–2433
10. Vallee BL, Auld DS (1990) *Biochemistry* 29:5647–5659
11. Parkin G (2000) *Chem Commun* 1971–1985
12. Parkin G (2004) *Chem Rev* 104:699–767
13. Nguyen KT, Wu J-C, Boylan JA, Gherardini FC, Pei D (2007) *Arch Biochem Biophys* 468:217–225
14. Becker A, Schlichting I, Kabsch W, Groche D, Schultz S, Wagner AFV (1998) *Nat Struct Biol* 5:1053–1058
15. Meinnel T, Blanquet S, Dardel F (1996) *J Mol Biol* 262:375–386
16. Fieulaine S, Juillan-Binard C, Serero A, Dardel F, Giglione C, Meinnel T, Ferrer J-L (2005) *J Biol Chem* 280:42315–42324
17. Escobar-Alvarez S, Goldgur Y, Yang G, Ouerfelli O, Li Y, Scheinberg DA (2009) *J Mol Biol* 387:1211–1228
18. Becker A, Schlichting I, Kabsch W, Schultz S, Wagner AFV (1998) *J Biol Chem* 273:11413–11416
19. Meinnel T, Lazennec C, Blanquet S (1995) *J Mol Biol* 254:175–183
20. Jain RK, Hao B, Liu RP, Chan MK (2005) *J Am Chem Soc* 127:4558–4559
21. Groche D, Becker A, Schlichting I, Kabsch W, Schultz S, Wagner AFV (1998) *Biochem Biophys Res Commun* 246:342–346
22. Ragusa S, Blanquet S, Meinnel T (1998) *J Mol Biol* 280:515–523
23. Wu X-H, Quan J-M, Wu Y-D (2007) *J Phys Chem B* 111:6236–6244
24. Xiao C, Zhang Y (2007) *J Phys Chem B* 111:6229–6235
25. Dong M, Liu H (2008) *J Phys Chem B* 112:10280–10290
26. Leopoldini M, Russo N, Toscano M (2006) *J Phys Chem B* 110:1063–1072
27. Chang SC, Karambelkar VV, diTargiani RC, Goldberg DP (2001) *Inorg Chem* 40:194–195
28. Chang SC, Sommer RD, Rheingold AL, Goldberg DP (2001) *Chem Commun* 2396–2397
29. Chang SC, Karambelkar VV, Sommer RD, Rheingold AL, Goldberg DP (2002) *Inorg Chem* 41:239–248
30. diTargiani RC, Chang SC, Salter MH, Hancock RD, Goldberg DP (2003) *Inorg Chem* 42:5825–5836
31. Goldberg DP, diTargiani RC, Namuswe F, Minnihan EC, Chang S, Zakharov LN, Rheingold AL (2005) *Inorg Chem* 44:7559–7569
32. Karambelkar VV, Xiao C, Zhang Y, Sarjeant AAN, Goldberg DP (2006) *Inorg Chem* 45:1409–1411
33. Otero A, Fernandez-Baeza J, Antinolo A, Tejada J, Lara-Sanchez A (2004) *Dalton Trans* 1499–1510
34. Hammes BS, Carrano CJ (1999) *Inorg Chem* 38:4593–4600
35. Hammes BS, Carrano CJ (2000) *J Chem Soc Dalton Trans* 3304–3309
36. Galardon E, Giorgi M, Artaud I (2007) *Dalton Trans* 1047–1052
37. PQS Version 3.3 (2006) Parallel Quantum Solutions, 2013 Green Acres Road, Fayetteville
38. Dolg M, Wedig U, Stoll H, Preuss H (1987) *J Chem Phys* 86:866–872
39. Baker J (1986) *J Comput Chem* 7:385–395
40. Glendening ED, Badenhop JK, Reed AE, Carpenter JE, Bohmann JA, Morales CM, Weinhold F (2001) NBO 5.0. Theoretical Chemistry Institute, University of Wisconsin, Madison. <http://www.chem.wisc.edu/~nbo5>
41. Klamt A, Schueuermann G (1993) *J Chem Soc Perkin Trans* 2:799–805
42. Andzelm J, Kolmel C, Klamt A (1995) *J Chem Phys* 103:9312–9320
43. Klamt A, Jonas V (1996) *J Chem Phys* 105:9972–9981
44. Balridge K, Klamt A (1997) *J Chem Phys* 106:6622–6633
45. Gilson MK, Honig BH (1986) *Biopolymers* 25:2097–2119
46. Cramer CJ (2004) *Essentials of computational chemistry: theories and models*, 2nd edn. Wiley, West Sussex
47. Tissandier MD, Cowen KA, Feng WY, Gundlach E, Cohen MH, Earhart AD, Coe JV, Tuttle TR (1998) *J Phys Chem A* 102:7787–7794
48. Kelly CP, Cramer CJ, Truhlar DG (2006) *J Phys Chem B* 110:16066–16081
49. Stewart R (1985) *The proton: applications to organic chemistry*. Academic Press, Orlando
50. Becke AD (1988) *Phys Rev A* 38:3098–3100
51. Lee CT, Yang WT, Parr RG (1988) *Phys Rev B* 37:785–789
52. Handy NC, Cohen AJ (2001) *Mol Phys* 99:403–412
53. Hamprecht FA, Cohen AJ, Tozer DJ, Handy NC (1998) *J Chem Phys* 109:6264–6271
54. Becke AD (1993) *J Chem Phys* 98:5648–5652
55. Cohen AJ, Handy NC (2001) *Mol Phys* 99:607–615
56. Becke AD (1997) *J Chem Phys* 107:8554–8560
57. Lide DR (2004) *Handbook of chemistry and physics*, 85th edn. CRC Press, Boca Raton
58. Solomon EI, Gorelsky SI, Dey A (2006) *J Comput Chem* 27:1415–1428